

A methodology for “modeling” the mechanical interaction between a reaction wheel and a flexible structure

Laila Mireille Elias^{*a}, Frank Dekens^{**b}, Ipek Basdogan^b, Lisa Sievers^b, and Tim Neville^b

^aMassachusetts Institute of Technology; ^bJet Propulsion Laboratory, California Institute of Technology

ABSTRACT

This paper presents a modeling methodology used to predict the performance of a flexible structure, such as a space telescope, in the presence of an on-board vibrational disturbance source, such as a reaction wheel assembly (RWA). Both *decoupled* and *coupled* analysis methods are presented. The *decoupled* method relies on blocked RWA disturbances, measured with the RWA hardmounted to a rigid surface. The *coupled* method corrects the blocked RWA disturbance boundary conditions using “force filters,” which depend on estimates of the interface *accelerances* of the RWA and spacecraft. Both methods were validated on the Micro-Precision Interferometer testbed at the Jet Propulsion Laboratory. Experimental results are encouraging, indicating that both methods provide sufficient accuracy compared to measured values; however, the coupled method provides the best results when the gyroscopic nature of the spinning RWA is captured in the RWA acceleration model. Additionally, the RWA disturbance cross spectral density terms are found to be influential.

Keywords: Dynamics, Vibrations, Disturbance Analysis, Coupling, Impedance, Reaction Wheel, Space Interferometry

NOMENCLATURE

<i>CSD</i>	Cross Spectral Density [N^2/Hz]	<i>FRF</i>	Frequency Response Function	<i>RMS</i>	Root Mean Square
<i>DAQ</i>	Data Acquisition System	<i>MPI</i>	Micro-Precision Interferometer	<i>RPM</i>	Revolutions Per Minute
<i>DOF</i>	Degree(s) of Freedom	<i>OPD</i>	Optical Pathlength Difference	<i>RWA</i>	Reaction Wheel Assembly
<i>FEM</i>	Finite Element Model	<i>PSD</i>	Power Spectral Density [N^2/Hz]	<i>SIM</i>	Space Interferometry Mission

1. INTRODUCTION

NASA’s future Space Interferometry Mission (SIM), depicted in Fig. 1, will be the first space-based optical interferometer. With optics mounted to its flexible truss structure, SIM must achieve nanometer-level stability requirements in the presence of on-board disturbances. The primary disturbance source anticipated for SIM is the reaction wheel assembly (RWA), a spinning flywheel assembly used for attitude control. In order to ensure mission success, a disturbance analysis method must be developed to predict SIM’s on-orbit performance in the presence of RWA disturbances.

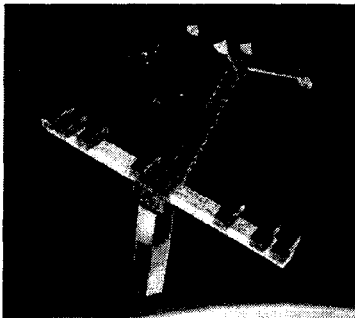


Fig. 1: NASA’s future Space Interferometry Mission.

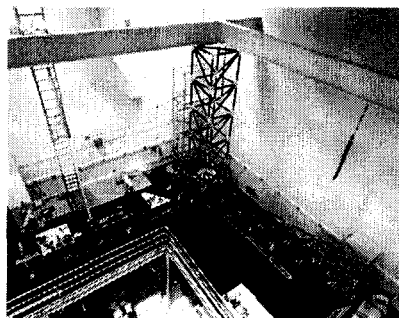


Fig. 2: The Micro-Precision Interferometer (MPI) testbed at the Jet Propulsion Laboratory.

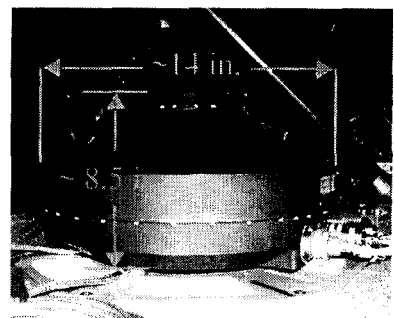


Fig. 3: RWA on the MPI base plate.

^{*}elias@mit.edu; <http://ssl.mit.edu>; MIT Space Systems Laboratory, 77 Mass. Ave., Room 37-354, Cambridge, MA, USA 02139

^{**}fdekens@jpl.nasa.gov; Jet Propulsion Laboratory, 4800 Oak Grove Drive, Pasadena, CA, USA 91109

RWA disturbances are typically measured in a “blocked” or “infinite-impedance” configuration, in which the RWA is hardmounted to a rigid surface and its interface is constrained to have zero motion. The RWA is spun, and a load transducer is used to measure the resulting disturbance loads at the interface. While this method provides consistent and repeatable boundary conditions, they are not an accurate representation of the coupled boundary conditions that occur when the RWA is mounted to a structure. In other words, the *blocked* RWA disturbances differ from the *coupled* disturbances that would actually exist at the spacecraft-RWA interface if the two bodies were coupled together.

This paper presents both a *decoupled* and a *coupled* disturbance analysis method used to predict the dynamic performance of a flexible structure, such as a space telescope, in the presence of on-board RWA vibrational disturbances. In the *decoupled* method, the blocked RWA disturbances are propagated through a spacecraft frequency response function (FRF) to predict the resulting spacecraft performance. In the *coupled* method, “force filters” are used to correct the blocked disturbances for the artificial boundary conditions imposed on the RWA during testing. The filters, which rely on estimates of the RWA and spacecraft interface *accelerances*, are used to “transform” the blocked RWA disturbances into the corresponding coupled disturbances. The coupled disturbances are then propagated, in place of the blocked disturbances, through a spacecraft FRF to predict the coupled performance. Both the decoupled and coupled analysis methods are validated by experimental data from the Micro-Precision Interferometer (MPI) testbed at the Jet Propulsion Laboratory.

1.1 The Micro-Precision Interferometer testbed

The MPI testbed, shown in its suspended configuration in Fig. 2, is a scale model of SIM. Like a space-based interferometer, MPI is a lightweight, flexible truss structure with mission-critical dynamics. Active optics, located on the left arm of the 7×6.5 meter boom assembly, are used to measure MPI’s performance in the presence of vibrational disturbances induced at the base of the three booms by an on-board RWA.¹ In this study, the performance metric of interest is the optical pathlength difference (OPD) between the two paths of the optical interferometer, usually expressed in nanometers.

Since the RWA is anticipated to be the largest disturbance source on SIM, the MPI disturbance analysis focuses on the disturbance path from the RWA vibrational inputs to the OPD. The RWA, shown hardmounted directly to the MPI base plate in Fig. 3, is similar to the one used for attitude control on the Magellan spacecraft. Although it is sometimes mounted on an isolator for research purposes, this paper focuses on the hardmounted configuration.

While the RWA is used to induce coupled, tonal disturbances characteristic of those expected on SIM, voice coil shakers, shown in Fig. 4, are alternatively used to induce “pure,” decoupled, white-noise forces and moments. These decoupled disturbances are useful for measuring the FRFs from the six loads (three forces and three moments) at the RWA mounting location to the OPD.



Fig. 4: Voice coil shakers on the MPI base.

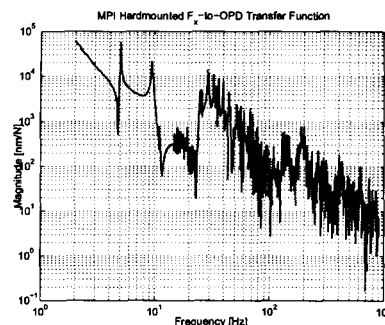


Fig. 5: MPI FRF: x-force-to-OPD.

1.2 The decoupled disturbance analysis method

The “traditional” or “decoupled” disturbance analysis method is based on a simple frequency-domain input-output principle. The MPI OPD is predicted for each wheel speed, Ω , as

$$Z(\omega, \Omega) = G_{ZF}(\omega)F(\omega, \Omega) \quad (1)$$

¹ Another metric for MPI is front-end pointing, expressed in milli-arcseconds and measured by a “position sensitive device.”

where ω represents frequency (in units of radians per second), Z is the $p \times 1$ *predicted performance* vector (in this case, the scalar OPD), F is an $n \times 1$ disturbance load vector (in this case, the 6×1 vector of measured RWA disturbance forces and moments), p is the number of performance metrics, and n is the dimension of the disturbance load vector. G_{ZF} is the $p \times n$ FRF of the structure (in this case, the 1×6 FRF relating disturbance loads at the RWA-mounting location on MPI to the OPD). The first component of G_{ZF} , the x -force-to-OPD FRF, is shown in Fig. 5.

Taking the expectation of the “square” of (1) allows us to write the analysis equation in terms of spectral density matrices:

$$\Phi_{ZZ}(\omega, \Omega) = G_{ZF}(\omega)\Phi_{FF}(\omega, \Omega)G_{ZF}^{*T}(\omega) \quad (2)$$

where Φ_{ZZ} is the predicted performance spectral density matrix (in this case, the scalar OPD power spectral density), Φ_{FF} is the RWA disturbance spectral density matrix (in this case, the 6×6 matrix with disturbance power spectra on the diagonal and cross-spectra off the diagonal), and $[\cdot]^{*T}$ denotes a complex-conjugate transpose operation.

From (2), we calculate the root mean square (RMS), σ_z , of the performance, Z , for each wheel speed, Ω :

$$\sigma_z(\Omega) = \sqrt{2 \int_0^{\omega_{max}} \Phi_{ZZ}(\omega, \Omega) d\omega} \quad (3)$$

When Z is a vector containing more than one performance metric, σ_z is a matrix whose diagonal components are the scalar RMS functions of the performances. When Z is a single performance (such as OPD), σ_z is its scalar RMS function.

An assumption is sometimes made that the diagonal terms of Φ_{FF} , or power spectral densities (PSDs), dominate the off-diagonal terms, or cross spectral densities (CSDs):

$$\Phi_{F_i F_i} \gg |\Phi_{F_i F_j}|, \quad i \neq j \quad (4)$$

When this holds true, Φ_{FF} is approximated as a diagonal matrix, and Equation (2) reduces from a fully populated *matrix equation* to a simple *summation of diagonal terms*:

$$\Phi_{ZZ}(\omega, \Omega) \approx \sum_{j=1}^6 \Phi_{F_i F_i}(\omega, \Omega) |G_{ZF_i}(\omega)|^2 \quad (5)$$

For each wheel speed, Ω , the OPD spectrum, Φ_{ZZ} , is approximated using (5), and its RMS is calculated using (3). To validate these predictions, the true OPD of the *coupled* MPI-RWA system is *measured* for each wheel speed with the RWA mounted on MPI. Fig. 6 shows the *predicted* and *measured* OPD RMS, both as functions of wheel speed.

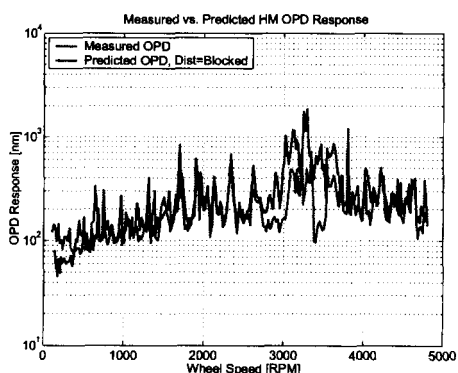


Fig. 6: Measured versus predicted OPD using blocked RWA disturbances.

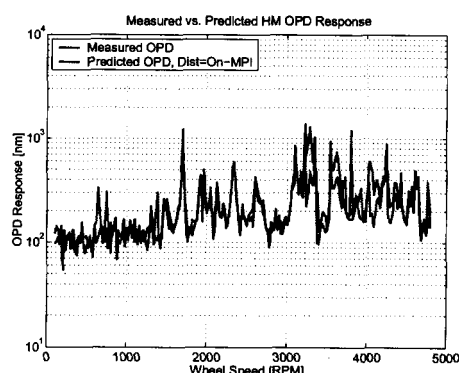


Fig. 7: Measured versus predicted OPD using coupled RWA disturbances.

1.3 Motivation for a “coupled” disturbance analysis method

The work documented in the remainder of this paper is motivated by the fact that the decoupled MPI performance predictions consistently overbound the measurements. This discrepancy has been, up to now, attributed to the decoupled nature

of the disturbance analysis method in (5). In propagating *blocked* RWA disturbances through an MPI FRF, *this method neglects the structural dynamic coupling between the MPI and RWA*. **Our goal is thus to correct the mismatch in RWA disturbance-testing boundary conditions by applying a coupling theory to the performance predictions on MPI. Reconciling the measured and predicted performances will affirm our ability to predict a spacecraft’s on-orbit dynamic behavior prior to flight.**

Previous MPI predictions have overbounded measurements by up to a factor of four, significantly more than shown in Fig. 6. Recent hardware modification have stiffened the MPI-RWA interface, both *decreasing* the amount of overprediction and *confining* it to the range of wheel speeds between 2700 and 3700 revolutions per minute (RPM). This confirms that dynamic coupling may be the critical aspect neglected by the decoupled method, since stiffening the interface effectively decreased the dynamic coupling between the two bodies and improved the prediction. Another indication that coupling is a concern is the fact that the OPD predicted using *coupled* disturbances, measured with the RWA mounted to MPI, in place of *blocked* disturbances yields much better results. Fig. 7 shows that using the *coupled* disturbances eliminates the overprediction at 2700-3200 and 3400-3500 RPM.

However, since there are still local regions in Fig. 7 (such as 3200-3400 and 3500-3700 RPM) where the analysis overpredicts the measurement, we consider other potential error sources. Aside from neglecting coupling, the disturbance analysis method in (5) makes other mathematical and physical approximations, such as neglecting the off-diagonal disturbance CSD terms in (2). Additionally, (5) fails to account for the gyroscopic stiffening effects of the spinning RWA. These factors will be discussed in Secs. 4 and 3.4 of this paper, respectively.

2. FORCE FILTER COUPLING METHOD

2.1 The force filter

In order to correct the mismatch of boundary conditions that occurs in blocked RWA disturbance testing, the following “force filter” relationship between the measured RWA blocked forces and the “true” coupled forces may be used:^{2,3}

$$\tilde{G}_{f,ii}(\omega) \equiv \frac{F_{c,i}(\omega)}{F_{b,i}(\omega)} = \frac{1}{1 + \frac{A_{MPI,ii}(\omega)}{A_{RWA,ii}(\omega)}} \quad , \quad i = 1, 2, 3 \quad (6)$$

where $i = 1, 2, 3$ refers to the $x, y,$ and z axes, respectively, ω represents frequency in radians per second, $\tilde{G}_{f,ii}$ is a “force filter” along the i^{th} axis, $F_{c,i}$ is the Fourier transform of the coupled interface force along the i^{th} axis, $F_{b,i}$ is the Fourier transform of the measured blocked force along the i^{th} axis, $A_{MPI,ii}$ is the MPI driving-point accelerance along the i^{th} axis, and $A_{RWA,ii}$ is the RWA driving-point accelerance along the i^{th} axis.*

Similarly, a “moment filter” can be written as

$$\tilde{G}_{f,ii}(\omega) \equiv \frac{M_{c,i}(\omega)}{M_{b,i}(\omega)} = \frac{1}{1 + \frac{A_{MPI,ii}(\omega)}{A_{RWA,ii}(\omega)}} \quad , \quad i = 4, 5, 6 \quad (7)$$

where $i = 4, 5, 6$ refers to *rotations about* the $x, y,$ and z axes, respectively, $M_{c,i}$ is the Fourier transform of the coupled interface *moment* along the i^{th} axis, $M_{b,i}$ is the Fourier transform of the measured blocked *moment* along the i^{th} axis, $A_{MPI,ii}$ is the MPI driving-point *rotational* accelerance about the i^{th} axis, and $A_{RWA,ii}$ is the RWA driving-point *rotational* accelerance about the i^{th} axis.

Table 1 lists the generalized input-output relationships between a load, F , imparted on a body and its resulting position, velocity, and acceleration: $Q, \dot{Q},$ and \ddot{Q} , respectively.⁴ (Where there is more than one acceptable term, the more common term is shown in bold.) From this table, it is clear that accelerance, A , is simply a derivative of mobility, Y :⁵

$$A(\omega) = \frac{\ddot{Q}(\omega)}{F(\omega)} = \frac{j\omega\dot{Q}(\omega)}{F(\omega)} = j\omega Y(\omega) \quad (8)$$

* The driving-point accelerance is a complex, frequency-dependent ratio of co-located acceleration and force at the interface, or “driving point” of a body. It is the inverse of the driving-point apparent mass. For more information, see reference 4.

TABLE 1: Generalized input-output relationships between a load and displacement, velocity, and acceleration.

Response/Load Ratios		Load/Response Ratios	
$\alpha(\omega) = \frac{Q(\omega)}{F(\omega)}$	Receptance, Admittance, Dynamic Compliance, Dynamic Flexibility	$\frac{1}{\alpha(\omega)} = \frac{F(\omega)}{Q(\omega)}$	Dynamic Stiffness
$Y(\omega) = \frac{\dot{Q}(\omega)}{F(\omega)}$	Mobility	$Z(\omega) = \frac{F(\omega)}{\dot{Q}(\omega)}$	Mechanical Impedance
$A(\omega) = \frac{\ddot{Q}(\omega)}{F(\omega)}$	Accelerance, Inertance	$\frac{1}{A(\omega)} = \frac{F(\omega)}{\ddot{Q}(\omega)}$	Apparent Mass, Dynamic Mass

and thus that the ratio of two bodies' *accelerances* is equivalent to the ratio of their *mobilities*:

$$\frac{A_{MPI,ii}}{A_{RWA,ii}} = \frac{j\omega Y_{MPI,ii}}{j\omega Y_{RWA,ii}} = \frac{Y_{MPI,ii}}{Y_{RWA,ii}} \quad (9)$$

Hence the filters in (6) and (7) can be formed using the ratio of MPI and RWA *accelerances* or *mobilities*:

$$\tilde{G}_{f,ii}(\omega) \equiv \frac{F_{c,i}(\omega)}{F_{b,i}(\omega)} = \frac{1}{1 + \frac{A_{MPI,ii}(\omega)}{A_{RWA,ii}(\omega)}} = \frac{1}{1 + \frac{Y_{MPI,ii}(\omega)}{Y_{RWA,ii}(\omega)}} \quad , \quad i = 1, 2, 3 \quad (10)$$

$$\tilde{G}_{f,ii}(\omega) \equiv \frac{M_{c,i}(\omega)}{M_{b,i}(\omega)} = \frac{1}{1 + \frac{A_{MPI,ii}(\omega)}{A_{RWA,ii}(\omega)}} = \frac{1}{1 + \frac{Y_{MPI,ii}(\omega)}{Y_{RWA,ii}(\omega)}} \quad , \quad i = 4, 5, 6 \quad (11)$$

2.2 The coupled disturbance analysis method

Recall from Equation (1) the input-output relationship used as the basis of the decoupled disturbance analysis method, where blocked disturbances are substituted for the actual interface forces, $F(\omega)$, applied to a spacecraft. Recall also the assumption that the disturbance PSDs dominate the CSDs, allowing us to approximate Equation (2) as (5). If we take the product of the blocked disturbances in (1) and the force and moment filters in (10) and (11), respectively, we effectively “filter” the blocked disturbances to yield the coupled disturbances. We can then rewrite the decoupled equation, (5), as a *coupled* analysis equation:

$$\Phi_{zz}(\omega, \Omega) \approx \sum_{j=1}^6 \Phi_{F,F_j}(\omega, \Omega) |\tilde{G}_{f,ii}(\omega)|^2 |G_{ZF_j}(\omega)|^2 \quad (12)$$

The $\Phi_{F,F_j}(\omega, \Omega) |\tilde{G}_{f,ii}(\omega)|^2$ terms represent the *filtered* or *coupled* disturbance PSDs. Using the coupled equation, (12), in place of the decoupled equation, (5), effectively corrects the mismatch of boundary conditions introduced by the blocked RWA disturbance testing. When force filters are available but moment filters are not (due to the difficulty in measuring rotational accelerances), (12) can be approximated by

$$\Phi_{zz}(\omega, \Omega) \approx \sum_{j=1}^3 \Phi_{F,F_j}(\omega, \Omega) |\tilde{G}_{f,ii}(\omega)|^2 |G_{ZF_j}(\omega)|^2 + \sum_{j=4}^6 \Phi_{F,F_j}(\omega, \Omega) |G_{ZF_j}(\omega)|^2 \quad (13)$$

where the moment filters have been set to unity, so that forces are filtered but moments are not.

Finally, we note an approximation inherent in (12). (12) was derived by directly “filtering” the blocked disturbance PSDs in (5), without considering the approximation made between (2) and (5). If, instead, we filter the original relation, (2), we

find a *matrix equation* analogous to (12) that contains not only the off-diagonal CSDs, $\Phi_{F_i F_j}$ for $i \neq j$, but also off-diagonal terms in G_f a fully populated force filter *matrix* formed from 6×6 RWA and MPI accelerance *matrices*.

The fully populated *force filter matrix*, analogous to the scalar force and moment filters in (10) and (11), respectively, is

$$G_f(\omega) = [I + A_{RWA}^{-1}(\omega)A_{MPI}(\omega)]^{-1}, \quad (14)$$

where I is the 6×6 identity matrix, and A_{RWA} and A_{MPI} are the 6×6 RWA and MPI accelerance matrices, respectively. Note that even using only the diagonal terms, $G_{f,ii}$ in (14) is not equivalent to $\tilde{G}_{f,ii}$ in (10), since (14) requires a *matrix inversion* of the fully-populated A_{RWA} matrix. In other words, the diagonals of $A_{RWA}^{-1}A_{MPI}$ in (14) are not the same as the scalar terms $A_{MPI,ii}/A_{RWA,ii}$ in (10). Hence $\tilde{G}_{f,ii}$ denotes an *approximation* of the diagonals, $G_{f,ii}$, of G_f .

The fully populated, coupled *matrix analysis equation*, analogous to the scalar equation, (12), is

$$\Phi_{zz}(\omega, \Omega) = G_{ZF}(\omega)G_f(\omega)\Phi_{FF}(\omega, \Omega)G_f^{*T}(\omega)G_{ZF}^{*T}(\omega). \quad (15)$$

For a complete derivation of these matrix equations, see reference 6. *While a matrix analysis using (14) and (15) is planned for MPI in the future, the work in the following section is based on the scalar analysis equations, (10)-(13).*

3. DISTURBANCE ANALYSIS VALIDATION

3.1 Initial coupled analysis

In order to test the coupled analysis theory, Equations (10) and (13) were implemented on MPI.⁷ The RWA is approximated as a rigid body with the equation of motion along each translational axis ($i = 1, 2, 3$):

$$f_i(t) = m_{RWA}\ddot{q}_i(t), \quad (16)$$

where f_i is the force acting on the RWA along its i^{th} axis, m_{RWA} is the RWA mass, and \ddot{q}_i is the RWA acceleration along the i^{th} axis. Taking the Fourier Transform of (16),

$$F_i(\omega) = m_{RWA}\ddot{Q}_i(\omega), \quad (17)$$

so that the RWA translational accelerances along the x, y , and z axes are

$$A_{RWA,ii}(\omega) = \frac{\ddot{Q}_i(\omega)}{F_i(\omega)} = \frac{1}{m_{RWA}}. \quad (18)$$

Substituting the RWA accelerances into Equation (10) yields the force filter for $i = 1, 2, 3$:

$$\frac{F_{c,i}}{F_{b,i}} = \frac{1}{1 + m_{RWA}A_{MPI,ii}}. \quad (19)$$

The RWA translational accelerances, based on Equation (18) and the measured RWA mass (8.885 kg), are shown in Fig. 8. Since they are frequency-independent, they have constant magnitudes equal to the inverse of the RWA mass.

The MPI translational accelerances, $A_{MPI,ii}$ for $i = 1, 2, 3$, were measured via tap tests. A Kistler Model 9728A20000 impulse hammer with a “soft” tip was used to tap MPI at the RWA mounting location in each of the three translational directions, and a Kistler Model 8628B5 accelerometer was used to measure the resulting accelerations. A Hewlett Packard 3566A data acquisition system (DAQ) was used to record and process the force and acceleration time histories. For each direction, five taps were performed, and the HP DAQ computed and averaged the resulting force-to-acceleration FRFs. The sampling rate was set at a maximum possible 12.6 kHz in order to capture the MPI dynamics during a very short (~0.01 second) impulse window. The resulting MPI translational accelerances are shown in Fig. 9.

The RWA mass and MPI translational accelerances are substituted into Equation (19) to yield the three translational force filters shown in Fig. 10. Because the filters are defined as ratios of coupled to blocked disturbances, their magnitudes are less than unity where the blocked loads *overpredict* the coupled ones, and greater than unity where the blocked loads *underpredict* the coupled ones. These filters, called the “rigid-RWA, tap-MPI” filters since they are based on rigid-body RWA accelerances and tap-test MPI accelerances, are now used to perform a disturbance analysis for MPI. This analysis is coupled in the translational degrees of freedom (DOF) only; in other words, Equation (13) is used to approximate (12),

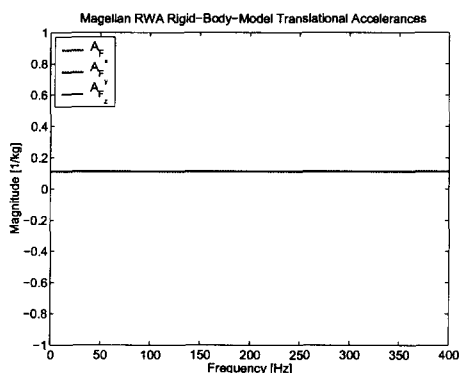


Fig. 8: RWA rigid-body-model translational accelerances.

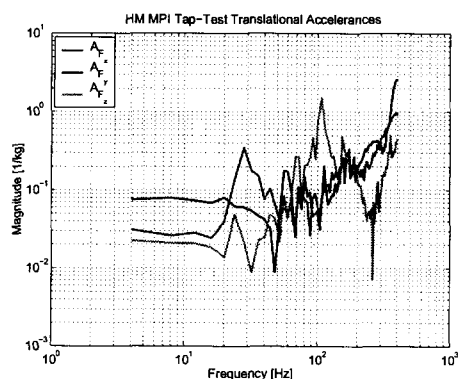


Fig. 9: MPI tap-test translational accelerances.

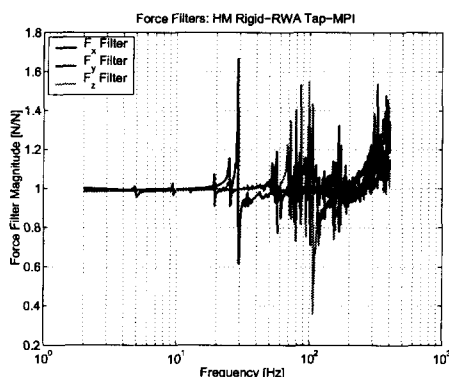


Fig. 10: Translational “rigid-RWA, tap-MPI” force filters.

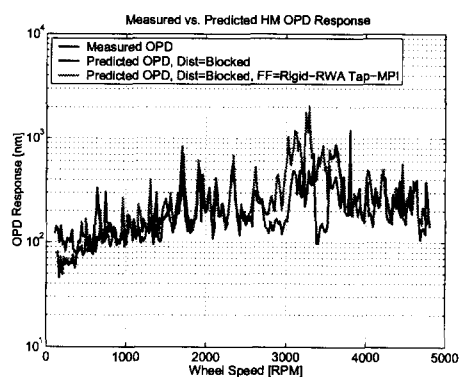


Fig. 11: Measured versus predicted OPD using blocked RWA disturbances and “rigid-RWA, tap-MPI” filters.

since the forces are filtered but the moments are not. The resulting coupled prediction is shown in Fig. 11, along with the decoupled prediction from Sec. 1.2 and the measured OPD.

The preliminary results in Fig. 11 are discouraging. The coupled and decoupled predictions are quite similar, both over-predicting the measured OPD in the 2700-3700 RPM range (where coupling was found to be of concern in Sec. 1.3). Thus the implementation of Equations (10) and (13) does not capture the coupling of the system.

We consider several reasons why this coupling method does not improve the decoupled analysis. First, we address concern about the quality of the MPI tap-test accelerance measurements. The accelerances in Fig. 9 are noisy, and because of the limited data-capture time window, limited data acquisition bandwidth, and poor signal coherence associated with impulsive tap tests, the MPI accelerance data are not of sufficient quality. Further, with a ~ 0.01 second impulse window, we cannot capture the sub-100 Hz dynamics of MPI. However, Fig. 5 shows that MPI is modally rich below 100 Hz.

Second, Equation (19) was used to filter the three forces, but the moment filters were neglected. This initial analysis was performed because there was no prior knowledge of the MPI rotational accelerances, and also because it was believed that the disturbance moments had a secondary contribution to the overall performance when compared with the forces.

Third, as described in Sec. 2.2, Equation (10) is only an exact relation for a single-DOF system, since it describes a ratio of coupled-to-blocked disturbances along a single axis. Although it can be applied sequentially to disturbance forces along the x , y , and z axes (and (11) can be applied to moments about the x , y , and z axes), it neglects coupling between the axes. Hence for most multi-DOF systems, it is only an approximation to matrix relation in (14). Similarly, Equations (12) and (13) are only approximations for the matrix relation in (15), since they neglect RWA disturbance CSDs.

Finally, the coupled analysis method neglects the gyroscopic effects caused by spinning bodies, such as the RWA fly-wheel. The remainder of this paper describes steps taken to reconcile the coupled predictions with the measured OPD by:

- obtaining more reliable MPI acceleration data
- accounting for RWA gyroscopic effects
- using moment filters, in addition to force filters
- including RWA disturbance CSDs, as well as PSDs.

3.2 Model-based accelerances

3.2.1 MPI model-based accelerance

Because the addition of the MPI accelerances via the force filter in Equation (19) did not reconcile the predicted and measured OPD values, potential error sources must be investigated. First, we address concern about the quality of the MPI tap-test accelerance data in Fig. 2.2. In order to eliminate error associated with the tap tests, we instead use a finite element model (FEM) of MPI to generate the desired accelerance data. An existing Integrated Modeling of Optical Systems (IMOS) model of MPI was used to generate the x , y , and z translational accelerances shown in Fig. 12. As expected, significant dynamics not captured in the tap tests lie below 100 Hz. Further, the magnitudes of the FEM-generated accelerances prove more accurate than the tap-test magnitudes. Treating the MPI as a rigid body at low frequency, we expect its accelerance to tend toward the inverse of its mass. Since the MPI mass is ~ 500 kg, its low-frequency accelerance should tend toward $2 \cdot 10^{-3} \text{ kg}^{-1}$. The FEM-based accelerances are consistent with this, particularly the x -axis translational accelerance.

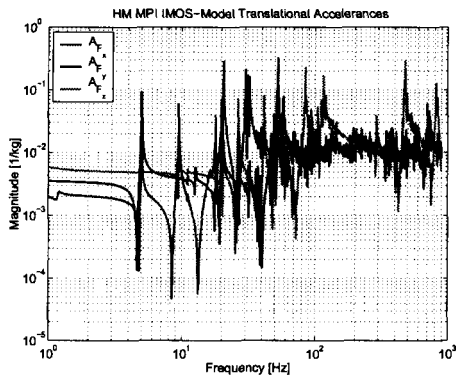


Fig. 12: MPI FEM-predicted translational accelerances.

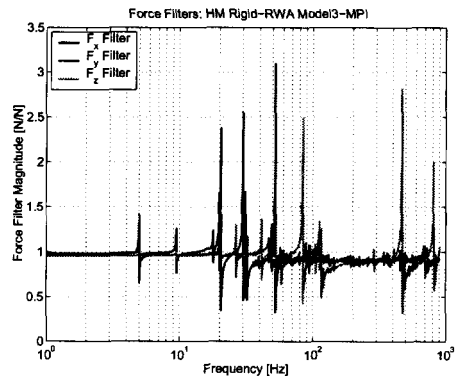


Fig. 13: Translational "rigid-RWA, model3-MPI" force filters.

The resulting force filters, based on the rigid-body-model RWA accelerance and the FEM-generated MPI accelerance, are shown in Fig. 13. They are referred to as "rigid-RWA, model3-MPI" filters. (The "3" in the filter name refers to the fact that we are still filtering the three forces, but not the moments.) Fig. 14 shows the resulting coupled OPD prediction, compared to both the decoupled prediction from Sec. 1 and the measured OPD. The decoupled and coupled predictions appear similar, and the coupled analysis is nearly identical to the "rigid-RWA, tap-MPI" analysis in Sec. 3.1, with very modest improvements. Hence, despite the improved quality in the MPI accelerances, these force filters do not significantly improve the OPD prediction, and the MPI accelerance data quality is probably not the primary factor contributing to the mismatch between prediction and measurement.*

3.2.2 MPI and RWA model-based rotational accelerances

Since the translational force filters do not improve the coupled OPD prediction, we now consider the rotational "moment" filters. Recall from Equation (11) that moment filters are formed from the ratio of RWA-to-MPI rotational accelerances. The RWA rotational accelerances can be generated from a rigid-body model, just as the RWA translational accelerances

* A study was also performed in which the three RWA translational accelerances were measured via tap tests. The resulting predictions provided no improvement over those in Fig. 14, confirming that the RWA flexibility is not influential in this analysis.

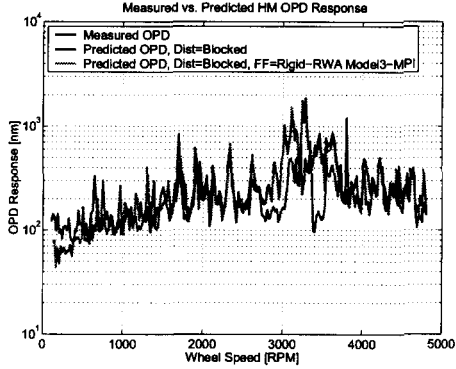


Fig. 14: Measured versus predicted OPD using blocked RWA disturbances and “rigid-RWA, model3-MPI” filters.

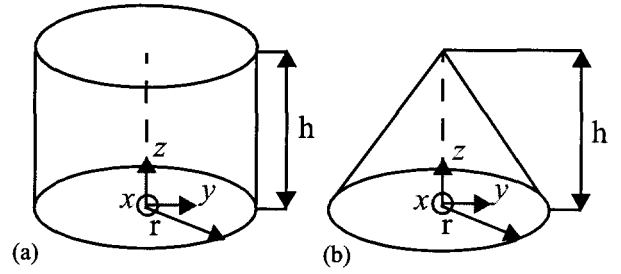


Fig. 15: Shapes used to estimate the Magellan RWA's mass moments of inertia: (a) cylinder and (b) cone.

are. The MPI rotational accelerances can be generated from the MPI FEM, just as the MPI translational accelerances are. Hence the rotational accelerances of both bodies can be derived from models.*

The RWA is treated as a rigid body with the rotational equation of motion about each axis ($i = 4, 5, 6$):

$$m_i(t) = I_{RWA,ii} \ddot{\theta}_i(t) , \quad (20)$$

where m_i is the moment acting on the RWA about its i^{th} axis, $I_{RWA,ii}$ is the RWA mass moment of inertia about its i^{th} axis, and $\ddot{\theta}_i$ is the RWA angular acceleration about its i^{th} axis. Taking the Fourier Transform of (20),

$$M_i(\omega) = I_{RWA,ii} \ddot{\Theta}_i(\omega) , \quad (21)$$

so that the RWA rotational accelerances about the $x, y,$ and z axes are

$$A_{RWA,ii} = \frac{\ddot{\Theta}_i}{M_i} = \frac{1}{I_{RWA,ii}} , \quad i = 4, 5, 6 . \quad (22)$$

Thus in order to calculate the RWA's *driving-point* rotational accelerances using (22), we must determine its moments of inertia, $I_{RWA,ii}$, about principal coordinate axes originating at the RWA-MPI interface point. Since inertia information is not available from the RWA manufacturer, the inertias are estimated from a constant-mass-density model.

From Fig. 3, we see the Magellan RWA lies somewhere between a cylindrical and conical shape. We can thus estimate the RWA inertia by averaging the inertias of a cylinder and a cone with similar mass and dimensions to the RWA. For the cylinder in Fig. 15(a), the moments of inertia are about the origin are

$$\begin{aligned} I_{xx} &= \frac{1}{12} m(3r^2 + h^2) \\ I_{yy} &= \frac{1}{12} m(3r^2 + h^2) , \\ I_{zz} &= \frac{1}{2} mr^2 \end{aligned} \quad (23)$$

and for the cone in Fig. 15(b),

* It is possible to *measure* the RWA and MPI rotational accelerances, but this generally requires a much more sophisticated test configuration and measurement techniques than tap tests allow, as demonstrated in reference 6.

$$\begin{aligned}
I_{xx} &= \frac{3}{80}m(4r^2 + h^2) \\
I_{yy} &= \frac{3}{80}m(4r^2 + h^2) \\
I_{zz} &= \frac{3}{10}mr^2
\end{aligned} \tag{24}$$

Substituting the RWA mass and dimensions into (23) and (24) and averaging the cylindrical and conical values, we obtain the RWA inertia estimates listed in Table 2. Although these values are approximate, any influence they might have will motivate the measurement of more accurate values or the direct measurement of the RWA rotational accelerances.

TABLE 2: Estimated mass moments of inertia [$\text{kg} \cdot \text{m}^2$] for the Magellan RWA.

$I_{\text{RWA},44}, I_{\text{RWA},55}$	0.0812
$I_{\text{RWA},66}$	0.1124

The RWA rotational accelerances, based on Equation (22) and the inertias in Table 2, are shown in Fig. 16. Since they are frequency-independent, they appear as constant lines, with magnitudes equal to the inverse of the RWA inertias. The MPI rotational accelerances, generated using the MPI FEM, are shown in Fig. 17. The resulting moment filters, based on the rigid-body-model RWA accelerance and FEM-generated MPI accelerance, are shown in Fig. 18, and are referred to as “rigid-RWA, model6-MPI” filters. (The “6” in the filter name refers to the fact that we are filtering *all six DOF*: moments, as well as forces.)

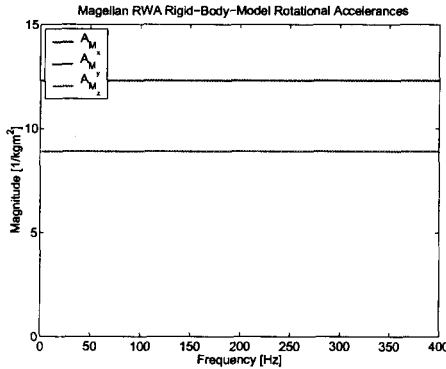


Fig. 16: RWA rigid-body-model rotational accelerances.

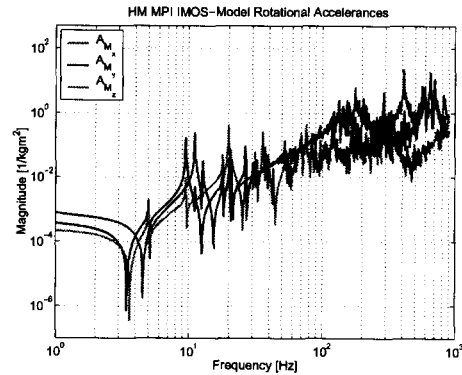


Fig. 17: MPI FEM-predicted rotational accelerances.

Fig. 19 shows the resulting coupled OPD prediction, using both the “rigid-RWA, model3-MPI” *force* filters and the “rigid-RWA, model6-MPI” *moment* filters. This prediction is compared to both the decoupled prediction from Sec. 1.2 and the measured OPD. The predictions due to the three-DOF and six-DOF filters in Figures 14 and 19, respectively, appear virtually indistinguishable, *indicating that the use of moment filters does not reconcile the predicted and measured OPD*.

3.3 Empirical force and moment filters

3.3.1 Motivation for empirical filters

The filters used so far have failed to improve upon the decoupled OPD prediction, as demonstrated by Figures 11, 14, and 19. Hence they must not actually transform the blocked disturbances into their coupled equivalents, and therefore must be incorrect. We now investigate “empirical filters,” which are formed from *measured disturbances* by taking the ratio of *coupled* disturbance spectra (measured with the RWA mounted on MPI) to *blocked* spectra. This ratio will provide an estimate of how the analytical filters *should* look.

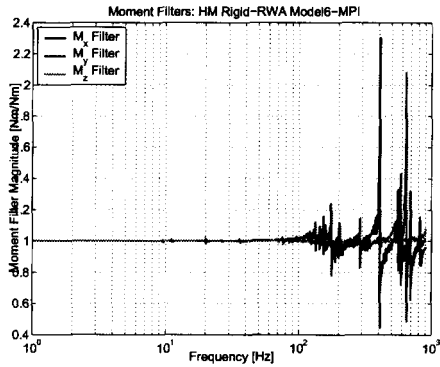


Fig. 18: Rotational “rigid-RWA, model6-MPI” moment filters.

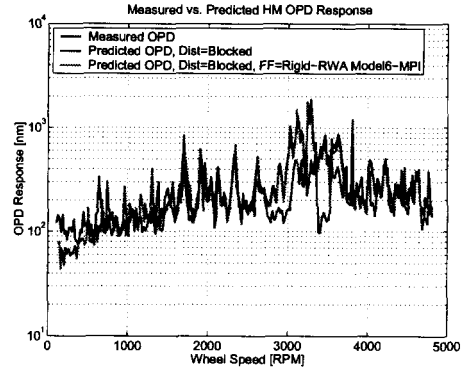


Fig. 19: Measured versus predicted OPD using blocked RWA disturbances and “rigid-RWA, model6-MPI” force and moment filters.

3.3.2 Empirical filter data

We form the three force and three moment empirical filters by dividing the coupled and blocked disturbance spectra. Since each spectrum, $\Phi_{F_i F_i}(\omega, \Omega)$ for $i = 1, 2, \dots, 6$, is a function of frequency (ω) and wheel spin rate (Ω), the resulting empirical filters are also frequency- and wheel-speed-dependent. The empirical F_x filter is shown in Fig. 20(a), and the M_x filter is shown in 20(b). Each filter is plotted as a function of frequency (x -axis) and wheel speed (y -axis), with its magnitude (in decibels) indicated by the neighboring color scale. The color-scale limits have been truncated to improve the signal-to-noise ratio; in other words, a few very large peaks have magnitudes “off” the scale and would eclipse the remaining data if the scale were normalized to the maximum values.

Large discrepancies exist between these empirical filters and the analytical filters in Sections 3.1 and 3.2. The empirical filters are highly dependent on wheel speed, while the “analytical” filters in Figs. 10, 13, and 18 depend only on frequency. Thus the analytical filters neglect some wheel-speed-dependent physics. Further, the empirical and analytical filters are quantitatively different. The empirical filter in Fig. 20(a), for example, has peak values over two orders of magnitude larger than its analytical equivalents in Figures 10 and 13. Similarly, the empirical filter in 20(b) has peak values over an order of magnitude larger than its analytical equivalent in Fig. 18.

While the qualitative difference between the empirical and analytical filters (namely, the wheel-speed-dependence of the empirical filters) is a factor we can investigate, the quantitative difference is more elusive because the empirical magnitudes are not entirely trustworthy. Since a blocked spectrum plotted in the frequency-versus-wheel-speed plane is mostly noise, with localized regions of signal due to tonal disturbances and structural modes of the RWA, an empirical filter is essentially the division of a coupled spectrum by noise *in all but the localized signal regions*. Hence the general trend of the empirical filters is correct, but the peak values are inaccurate.

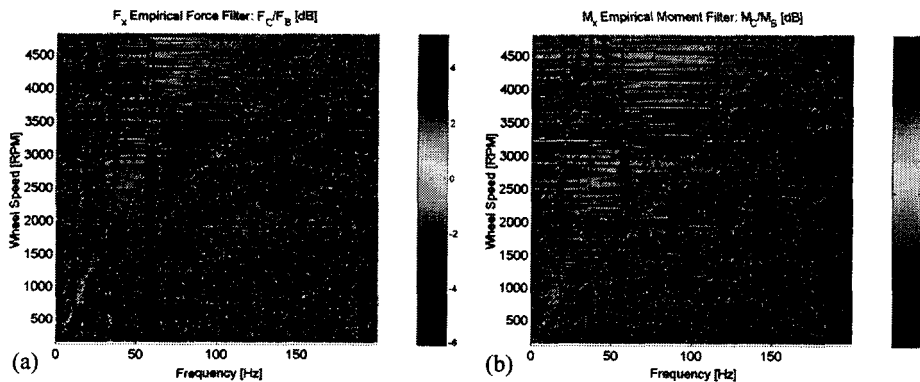


Fig. 20: Empirical filters: (a) F_x empirical force filter, (b) M_x empirical moment filter.

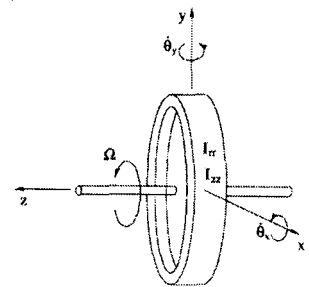


Fig. 21: Rigid flywheel model.

It would be useful to improve the numerical accuracy of the empirical filters in the future, but for now, we confirm their general correctness by using them in a coupled disturbance analysis. Since the empirical filters are the true ratios of coupled-to-blocked disturbance spectra, filtering the blocked spectra should return the coupled spectra, and the resulting filtered prediction should be identical to an unfiltered prediction using the coupled spectra. Previous analyses have demonstrated this, so despite concerns about the peak magnitudes, we know the empirical filters are somewhat correct.⁸

3.4 Addition of RWA gyroscopic terms

We have found the unexpected result that the empirical filters depend highly on the wheel's spin rate. However, the analytical filters in Sections 3.1 and 3.2, formed using Equations (10) and (11), are independent of wheel speed as long as the MPI and RWA accelerances are independent of wheel speed. Clearly the MPI accelerance is independent of wheel speed, yet this is not true for the RWA accelerance, which is influenced by gyroscopic effects. An attempt is now made to account for "gyroscopic stiffening" effects in the RWA accelerance models.

Consider the symmetric, rigid, spinning flywheel in Fig. 21. Its rotational equations of motion about the radial axes are:²

$$\begin{bmatrix} I_{rr} & 0 \\ 0 & I_{rr} \end{bmatrix} \begin{Bmatrix} \ddot{\theta}_x \\ \ddot{\theta}_y \end{Bmatrix} + \begin{bmatrix} 0 & \Omega I_{zz} \\ -\Omega I_{zz} & 0 \end{bmatrix} \begin{Bmatrix} \dot{\theta}_x \\ \dot{\theta}_y \end{Bmatrix} = \begin{Bmatrix} m_x \\ m_y \end{Bmatrix}, \quad (25)$$

where I_{rr} is the mass moment of inertia about the radial axes, I_{zz} is the mass moment of inertia about the spin axis, Ω is the flywheel's spin rate, θ_x and θ_y are the angular rotations about the x and y axes, respectively, and m_x and m_y are external moments applied about the x and y axes, respectively. Notice the skew-symmetric damping matrix with two off-diagonal, wheel-speed-dependent terms: ΩI_{zz} and $-\Omega I_{zz}$. These are the gyroscopic terms of interest.

Taking the Fourier Transform of (25), using (8) to write velocities in terms of accelerations, and collecting terms,

$$\begin{bmatrix} I_{rr} & \frac{\Omega I_{zz}}{j\omega} \\ \frac{-\Omega I_{zz}}{j\omega} & I_{rr} \end{bmatrix} \begin{Bmatrix} \ddot{\Theta}_x \\ \ddot{\Theta}_y \end{Bmatrix} = \begin{Bmatrix} M_x \\ M_y \end{Bmatrix}. \quad (26)$$

Equation (26) can now be solved to yield the flywheel's rotational accelerations in terms of the moments:

$$\begin{Bmatrix} \ddot{\Theta}_x \\ \ddot{\Theta}_y \end{Bmatrix} = \begin{bmatrix} I_{rr} & \frac{\Omega I_{zz}}{j\omega} \\ \frac{-\Omega I_{zz}}{j\omega} & I_{rr} \end{bmatrix}^{-1} \begin{Bmatrix} M_x \\ M_y \end{Bmatrix}, \quad (27)$$

so that the coupled *rotational accelerance* of the wheel about its x - and y -axes is:

$$\boxed{\begin{bmatrix} I_{rr} & \frac{\Omega I_{zz}}{j\omega} \\ \frac{-\Omega I_{zz}}{j\omega} & I_{rr} \end{bmatrix}^{-1} = \frac{1}{(I_{rr})^2 - \left(\frac{\Omega I_{zz}}{\omega}\right)^2} \begin{bmatrix} I_{rr} & -\frac{\Omega I_{zz}}{j\omega} \\ \frac{\Omega I_{zz}}{j\omega} & I_{rr} \end{bmatrix}}. \quad (28)$$

We would like to substitute this accelerance in place of the expression in (22) (for $i = 4, 5$), which does *not* include gyroscopic effects. However, like all the accelerances used so far in this study, the accelerances in (22) are decoupled between the axes. Accordingly, all the MatlabTM code developed to implement the filters is based on (10) and (11), rather than on (14), and considerable effort is required to modify the code to include off-diagonal accelerance terms in the filters. Hence we approximate the RWA accelerance in (28) as having only its diagonal terms. *We recognize that gyroscopic effects are highly coupled between the axes and that the off-diagonal accelerance terms may be quite influential; a full investigation*

of these terms is planned in the future. For now, we recognize that these diagonal terms are *still an improvement over the RWA rotational accelerances* in (22), since they now depend on RWA wheel-speed.

From Equations (27) and (28), if only M_x is applied, the rotational accelerance about the x -axis is:

$$\frac{\ddot{\Theta}_x}{M_x} = \frac{I_{rr}}{(I_{rr})^2 - \left(\frac{\Omega I_{zz}}{\omega}\right)^2}, \quad (29)$$

and if only M_y is applied, the rotational accelerance about the y -axis is:

$$\frac{\ddot{\Theta}_y}{M_y} = \frac{I_{rr}}{(I_{rr})^2 - \left(\frac{\Omega I_{zz}}{\omega}\right)^2}. \quad (30)$$

These “gyroscopic” rotational accelerances depend on both frequency and wheel speed, as expected. When the wheel is at rest ($\Omega=0$), it is easily shown that (29) and (30) reduce to (22) (for $i = 4, 5$), the RWA rotational accelerances *without* gyroscopic effects.

(29) and (30) are now substituted into (11), along with the MPI FEM-generated rotational accelerances, to yield the “rigid-gyro-RWA, model6-MPI” moment filters that *include gyroscopic effects and depend on both frequency and wheel speed* but neglect off-axis terms. The resulting moment filters are shown in Fig. 22. Although they now depend on wheel speed, their peak magnitudes are still much smaller than the empirical filters in Sec. 3.3. Also, their dependence on wheel speed appears qualitatively different from the empirical filters. The gyroscopic filters increase roughly as wheel speed squared, and this wheel-speed dependence appears only at low frequencies (under 20 Hz); however, the empirical moment filter in Fig. 20 has a non-deterministic dependence on wheel speed, and this dependence occurs over a broad frequency range (0-150 Hz).

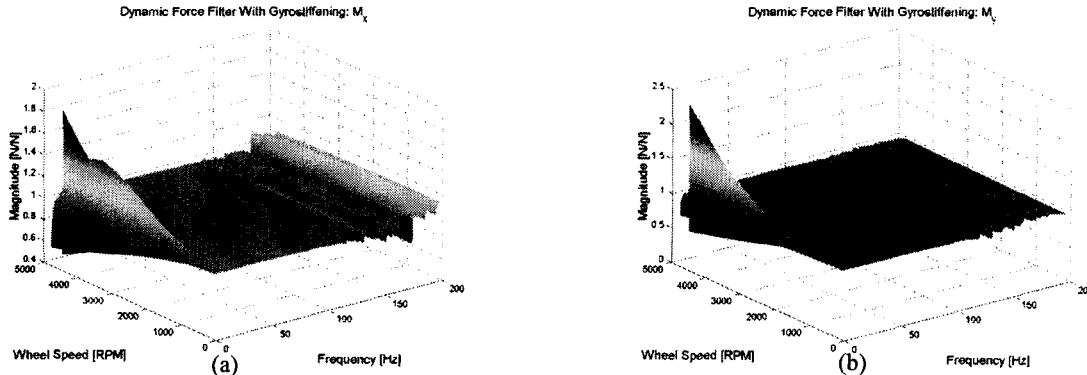


Fig. 22: “Rigid-gyro-RWA, model6-MPI” moment filters: (a) M_x filter and (b) M_y filter.

Despite these discrepancies, the analysis performed with the gyroscopic filters *does* improve the coupled OPD prediction. Fig. 23, shows the coupled prediction using both the “rigid-RWA, model3-MPI” *force* filters and the “rigid-gyro-RWA, model6-MPI” *moment* filters. This coupled prediction is compared to both the decoupled prediction from Sec. 1.2 and the measured OPD. The gyroscopic filters improve upon the decoupled prediction significantly between 3050 and 3200 RPM, as well as near 3400 and 3500 RPM. **Hence the gyroscopic moment filters improve the coupled analysis method more than any other filters so far.**

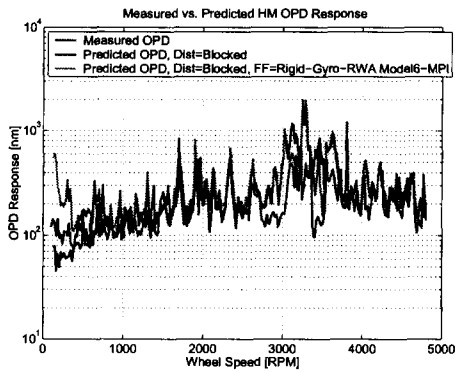


Fig. 23: Measured versus predicted hardmounted OPD response using blocked RWA disturbances and the “rigid-gyro-RWA, model6-MPI” force and moment filters.

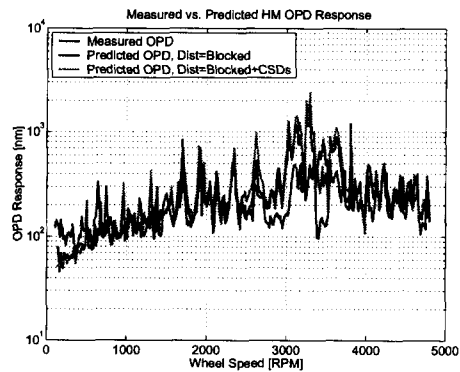


Fig. 24: Measured versus predicted hardmounted OPD response using blocked RWA disturbance PSDs and CSDs (without force and moment filters).

4. ADDITION OF CROSS-SPECTRAL-DENSITY (CSD) DISTURBANCE TERMS

One final approximation in the coupled analysis method is now investigated. Recall the simplification from the coupled matrix equations, (14) and (15), to the scalar equations, (10)-(12). The latter equations neglect two types of off-diagonal terms:

- the off-diagonal terms in the RWA and MPI accelerance matrices and
- the off-diagonal terms in the RWA disturbance spectral density matrix (the CSDs).

Accounting for the first set of terms would be difficult, since measuring a body’s 6×6 accelerance matrix is not trivial and may require considerable resources. Even if MPI’s accelerance matrix were generated from a FEM, it would still be necessary to measure the RWA accelerance matrix. We focus instead on the latter terms, the RWA disturbance CSDs.

Matlab™ code, originally written to calculate PSDs from RWA disturbance time histories, was modified to also calculate CSDs. The coupled disturbance analysis code, originally based on Equations (10)-(12) (or (10) and (13)), was modified to use Equation (15) in place of (12), hence including the RWA disturbance CSDs (the off-diagonal terms in Φ_{FF}). The modified analysis code, however, still uses the scalar force and moment filters in (10) and (11) (compiled into a 6×6 diagonal matrix, \tilde{G}_f), instead of the fully populated force filter matrix, G_f , in (14), since RWA and MPI accelerance matrices are not available.

To isolate the effect of the disturbance CSDs (without accounting for coupling), a *decoupled* analysis including CSDs was performed using (15) by setting the force filter matrix, G_f , equal to the 6×6 identity matrix (equivalent to using the unfiltered matrix expression in (2)). The resulting OPD prediction is shown in Fig. 24, along with the measured OPD and the decoupled prediction using only PSD terms. Fig. 24 demonstrates that including the disturbance CSDs improves the decoupled OPD prediction in some regions (particularly near 3450-3550 RPM), yet degrades the prediction in other regions, such as near 2600 RPM.* Since this is a decoupled prediction, and the improvement is *due simply to the addition of disturbance CSDs*, it is recommended in future analyses, whether decoupled or coupled, to include RWA disturbance CSDs in the analysis equations.

5. CONCLUSIONS

Experimental validation on the MPI testbed indicates that both the *decoupled* and *coupled* disturbance analysis methods presented in this paper provide sufficient accuracy compared to measured performances. However, the coupled analysis method provides improved results when the gyroscopic nature of the spinning RWA is captured in the RWA accelerance model, especially in certain wheel-speed ranges where MPI-RWA coupling is influential. **Hence inclusion of RWA gyroscopic effects is recommended in a coupled spacecraft-RWA disturbance analysis.**

*A similar study, however, has shown that CSD terms cause a *significant* improvement for the isolated-RWA configuration on MPI.

Additionally, the inclusion of RWA disturbance CSDs in Sec. 4 improves the OPD prediction significantly in certain regions, despite adversely affecting the prediction in other localized regions. **Because of their influence, RWA disturbance CSDs should be retained in future disturbance analyses.**

Finally, **an investigation of the influence of the fully populated RWA and MPI accelerance matrices** (and thus the filter *matrix* in Equation (14)) should be performed in the future; the off-diagonal terms neglected in the gyroscopic filter analysis in Sec. 3.4 should also be incorporated.

ACKNOWLEDGMENTS

This work was performed at the Massachusetts Institute of Technology and in part at the Jet Propulsion Laboratory, California Institute of Technology under contract with the National Aeronautics and Space Administration.

REFERENCES

1. J.W. Melody and G.W. Neat, "Integrated Modeling Methodology Validation Using the Micro-Precision Interferometer Testbed," *Proceedings of the 35th IEEE Conference on Decision and Control* 4, pp. 4222-4227, December 1996.
2. L.M. Elias, "Validation of a Coupled Reaction Wheel Disturbance Analysis Method for the MPI Testbed at JPL. Summary of Work: June 2001 - May 2002," *Jet Propulsion Laboratory Internal Document: Unofficial Interoffice Memorandum*, May 31, 2002.
3. S.R. Ploen, "Analysis of MPI/RWA Dynamic Coupling via Mechanical Impedance Methods," *Jet Propulsion Laboratory Engineering Memorandum 3455-01-001*, January 4, 2001.
4. D.J. Ewins, *Modal Testing: Theory, Practice, and Application*, Second Edition, Research Studies Press Ltd., 2000.
5. L.M. Elias, *A Structurally Coupled Disturbance Analysis Method Using Dynamic Mass Measurement Techniques, with Application to Spacecraft-Reaction Wheel Systems*, Master's thesis, Massachusetts Institute of Technology, March 2001.
6. L.M. Elias, "A Coupled Disturbance Analysis Method Using Dynamic Mass Measurement Techniques," *Proceedings of the 43rd Annual AIAA/ASME/ASCE/AHS/ASC Structures, Structural Dynamics, and Materials Conference*, April 2002. AIAA Paper 2002-1252.
7. R. Grogan, "Summary of Reaction Wheel Analysis Validation," *Jet Propulsion Laboratory Internal Document: Interoffice Memorandum 3411-01-000 SIM*, July 2, 2001.
8. L.M. Elias, "Summary of Work: JPL Summer 2001," *Jet Propulsion Laboratory Internal Document: Unofficial Interoffice Memorandum*, August 31, 2001.
9. N.M.M. Maia, J.M.M. Silva, J. He, N.A.J. Lieven, R.M. Lin, G.W. Skingle, W. To, and A.P.V. Urgueira, *Theoretical and Experimental Modal Analysis*, Research Studies Press Ltd., 1997.
10. P.H. Wirsching, T.L. Paez, and H. Ortiz, *Random Vibrations: Theory and Practice*, John Wiley & Sons, Inc., 1995.